Nucl. Part. Phys. Proc. xxx (xxxx) xxx

Contents lists available at ScienceDirect

Nuclear and Particle Physics Proceedings

journal homepage: www.elsevier.com/locate/nppp

Multi-differential measurement of the dijet cross section in proton-proton collisions at $\sqrt{s} = 13$ TeV

Polidamas Georgios Kosmoglou Kioseoglou * on behalf of the CMS Collaboration

University of Ioannina, university of Ioannina 45110, Greece

ARTICLE INFO

Keywords:
SM
Proton
Jets
QCD
pQCD
PDFs

ABSTRACT

A measurement of the dijet production cross section is reported based on an integrated luminosity of 36.3 fb^{-1} of proton–proton collision data collected in 2016 at $\sqrt{s} = 13$ TeV by the CMS detector [2] at the CERN LHC. Jets are reconstructed with the anti-k$_T$ algorithm for distance parameters of $R = 0.4$ and $R = 0.8$ and differential cross sections are measured as a function of the kinematic properties of the two jets with largest transverse momenta p_T. Double-differential (2D) measurements are presented as a function of the largest absolute rapidity $|y|_{max}$ of the two jets and the dijet invariant mass $m_{1,2}$. Triple-differential (3D) measurements are presented as a function of the dijet rapidity separation $y*$, the total boost y_b of the dijet system, and either $m_{1,2}$ or the average dijet transverse momentum $\langle p_T \rangle_{1,2}$ as the third variable. The measured cross sections are unfolded to correct for detector effects and are compared with fixed-order calculations derived at next-to-next-to-leading order in perturbative quantum chromodynamics. The impact of the 2D and 3D measurements is investigated on the determination of the parton distribution functions (PDFs) and the strong coupling constant (α_S), with the inclusion of the 3D cross sections yielding the more precise value of $\alpha_S(m_Z) = 0.1201 \pm 0.0020$.

1. Dijet measurements

Jets belong among the most frequent objects encountered in high energy proton-proton (pp) collisions. They provide a great window on the underlying physics between the elementary particles that comprise them and their interactions. Precise dijet measurements are exploited to further constrain existing PDFs and study the α_S.

The double-differential (2D) measurement is performed as a function of the largest absolute rapidity $|y|_{max}$ of the two jets with the largest p_T in the event and their invariant mass $m_{1,2}$. The triple-differential (3D) measurement is then taken as a function of the rapidity separation $y^* = |y_1 - y_2|/2$, the total boost of the dijet system $y_b = |y_1 + y_2|/2$ and either the invariant mass $m_{1,2}$ or the average transverse momentum $\langle p_T \rangle_{1,2}$ of the two jets.

The anti-k$_T$ clustering algorithm [1] is used for the jet reconstruction for two different values of the jet distance parameter R, a smaller one of 0.4 and a larger one of 0.8, amounting to six dijet measurements in total.

1.1. Phase space

The data were recorded at 2016 by the CMS detector [2] at the CERN LHC, at pp collisions at $\sqrt{s} = 13$ TeV and correspond to an integrated luminosity of $\mathcal{L}_{int} = 36.3$ fb^{-1}. Simulated samples are generated with the Pythia8 [3] Monte Carlo (MC) event generator at LO in perturbative quantum chromodynamics (pQCD), the CUETP8M1 [4] tune is used to emulate the hadronization and the multi parton interactions, while to study the impact of the detector response the samples are processed through the GEANT4 package [5].

During the offline analysis the phase space is further restricted so that the two leading jets, respectively, in each event have $p_{T,1} \geq 100$ GeV, $p_{T,2} \geq 50$ GeV and $|y_1| < 2.5\,(3.0)$, $|y_2| < 2.5\,(3.0)$ for the 2D (for the 3D) measurement.

1.2. Particle level distributions

Selection criteria are applied to the samples, jet transverse momentum and energy are calibrated and known detector effects that caused

* Corresponding author.
E-mail address: polidamas.kosmoglou@cern.ch (P.G. Kosmoglou Kioseoglou).

https://doi.org/10.1016/j.nuclphysbps.2023.09.010
Received 13 September 2023; Accepted 22 September 2023

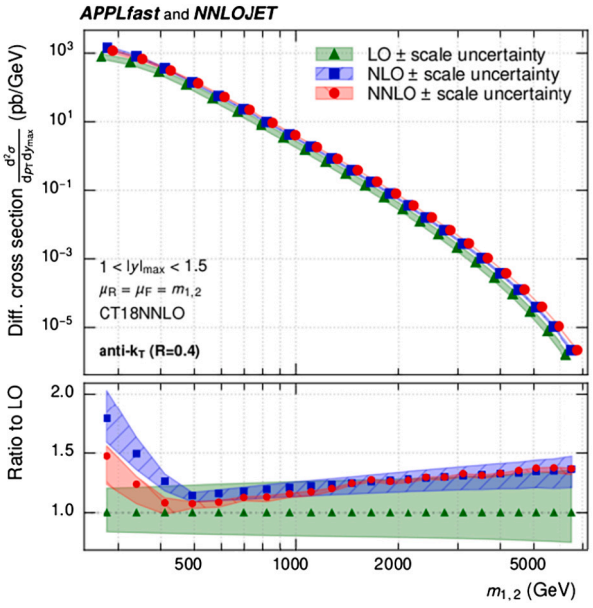

Fig. 1. Fixed order predictions at NNLO for the 2D cross section as a function of $m_{1,2}$ [10].

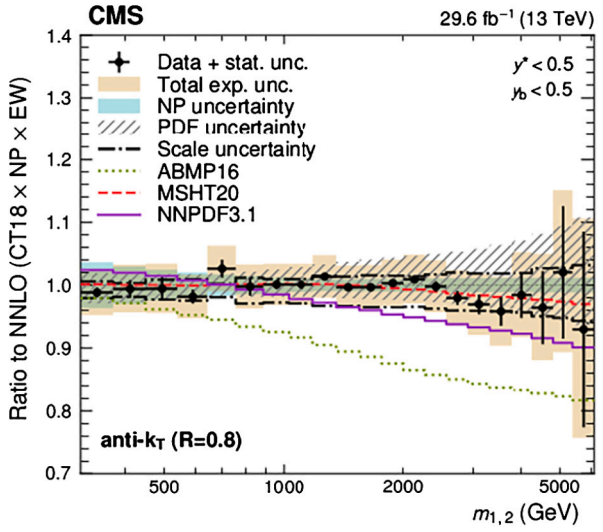

Fig. 2. Ratio of data over theory for the 3D cross section as a function of $m_{1,2}$ [20].

inefficiencies in certain phase space regions are taken into account. Additionally, simulated samples are reweighted to properly describe the pileup profile observed in data, smeared due to the finite detector resolution and cleaned from unphysical overweighted events, artifacts from the sample generation stage.

Multi-differential unfolding is performed to obtain the particle level cross sections, a procedure aimed to reverse event migrations caused by the finite detector resolution during the online data collection. Event migrations are treated among all observable bins. The TUnfold [6] package is used following a least square minimization within the pseudo-matrix inversion approach. The input probability matrix required for unfolding is constructed from the simulated samples by calculating $m_{1,2}$ two times, once at generator level and once at reconstructed level, a matrix that depicts the probability of an event to migrate from one level to the other.

1.3. Experimental uncertainties

Statistical uncertainties are propagated through the unfolding procedure resulting in non-negligible correlations in the final cross sections. Systematic effects are estimated similarly for both the data and the simulated samples. In the case of data, experimental parameters are varied within $a \pm 1\sigma$ around the nominal value. Resulted distributions are unfolded by the default probability matrix where the difference between the output distributions to the nominal one is taken as an asymmetric uncertainty in the output cross sections. In the case of MC, again, experimental parameters are varied, this time, resulting in different probability matrices. The nominal data cross sections are then unfolded by each one of the produced matrices, once again, taking their respective differences as the final asymmetric uncertainty.

2. Fixed order theory predictions

Fixed order (FO) predictions are obtained with the NNLOJET program [7] (revision 5918) as FASTNLO [8,9] (version 2.3) interpolation grids within the APPLFAST interface [10] (version 0.046). The calculation is performed at next-to-next-to-leading order (NNLO) accuracy in pQCD where the renormalization and factorization scales have been chosen to be equal to $\mu_R = \mu_F = m_{1,2}$ (Fig. 1).

The matrix element is combined with the CT18 (at NNLO) PDF set [11], while the resulted cross sections are additionally corrected to account for nonperturbative (NP) effects (hadronization and multi parton interactions) and extra electroweak (EW) radiation (virtual exchange of soft or collinear $W^{\pm}$ or Z bosons) [12]. It is noted that the current predictions are based in the leading-color (N_C) and leading-flavor-number (N_F) approximations [13,14]. Subleading-color contributions have not yet been tried for this set of observables so their impact still remains unknown, thus these measurements provide ideal testing grounds to hold such studies.

Theory uncertainties are decomposed into three different sources, namely the scale, PDF and NP, where the total one is calculated as the quadrature of the aforementioned ones. A scale uncertainty is introduced to account for the missing higher orders in pQCD and is estimated from a six scale variation of μ_R, μ_F around their nominal values as $(1/2,\ 1/2)$, $(1/2,\ 1)$, $(1,\ 1/2)$, $(2,\ 1)$, $(1,\ 2)$, and $(2,\ 2)$. The PDF uncertainty is taken as 68% confidence intervals following the prescriptions as given in the respective reference. Lastly, the NP uncertainty is calculated by taking the envelope of the nonperturbative contribution as estimated by different MC event generators.

2.1. Data to theory comparison

The experimental data are compared to the NNLO predictions, where the agreement is found to be good, remaining below 10% in most phase space regions within respective uncertainties, for all six measurement configurations. Best agreement is generally displayed by the larger jet cone size ($R = 0.8$). Fixed order predictions are additionally combined with other PDF sets, namely ABMP16 [15], MSHT20 [16] and NNPDF3.1 [17], and compared to the CT18 baseline. The better agreement to the CT18 PDF set is found by the MSHT20 (Fig. 2).

3. QCD analysis

Quantum chromodynamics analysis is performed once with the inclusion of the double-differential cross section and once with the inclusion of the triple-differential one. The chosen measurements are the ones given as a function of $m_{1,2}$ to reach the higher end of the phase space while using the larger jet cone size ($R = 0.8$) to profit from the increased agreement displayed by the NNLO pQCD predictions. The strategy followed is the same as in past HERAPDF analysis [18] where HERA deep inelastic scattering (DIS) data are used and are complemented with the CMS dijet cross sections.

Table 1
PDF parametrization obtained after the x^2 minimization scan for the fits of HERA DIS data together with the CMS 2D or 3D dijet cross sections [20].

PDF	Fitted data sets	
	HERA DIS + CMS dijets (2D)	HERA DIS + CMS dijets (3D)
$xg(x,\ \mu^2_{F,0})$	$A_g x^{B_g}(1-x)^{C_g}$	$A_g x^{B_g}(1-x)^{C_g}$
$xu_v(x,\ \mu^2_{F,0})$	$A_{u_v} x^{B_{u_v}}(1-x)^{C_{u_v}}(1+D_{u_v}x+E_{u_v}x^2)$	$A_{u_v} x^{B_{u_v}}(1-x)^{C_{u_v}}(1+D_{u_v}x)$
$xd_v(x,\ \mu^2_{F,0})$	$A_{d_v} x^{B_{d_v}}(1-x)^{C_{d_v}}$	$A_{d_v} x^{B_{d_v}}(1-x)^{C_{d_v}}$
$x\overline{U}(x,\ \mu^2_{F,0})$	$A_{\overline{U}} x^{B_{\overline{U}}}(1-x)^{C_{\overline{U}}}(1+D_{\overline{U}}x)$	$A_{\overline{U}} x^{B_{\overline{U}}}(1-x)^{C_{\overline{U}}}(1+D_{\overline{U}}x)$
$x\overline{D}(x,\ \mu^2_{F,0})$	$A_{\overline{D}} x^{B_{\overline{D}}}(1-x)^{C_{\overline{D}}}$	$A_{\overline{D}} x^{B_{\overline{D}}}(1-x)^{C_{\overline{D}}}(1+D_{\overline{D}}x)$

Both PDF-only (with $\alpha_S(m_Z) = 0.118$ fixed) and PDF+α_S fits are performed with the xFitter program (version 2.0.1) [19] interfaced to fastNLO. The PDFs are parametrized to the proton momentum fraction x as:

$$xf(x,\mu^2_{F,0}) = A_f x^{B_f}(1-x)^{C_f}(1+D_f x+E_f x^2) \quad (1)$$

where f corresponds to the individual distributions that express the proton structure, namely the gluon distribution $g(x)$, the up and down valence quark distributions $u_v(x)$, $d_v(x)$ and the up- and down-type sea antiquark distributions $\overline{U}(x)$, $\overline{D}(x)$. Parton distribution functions are determined at a starting scale of $\mu_{F,0} = 1.9$ GeV^2 and are then evolved at the scale of the top quark mass m_t.

The fit procedure starts with 10 parameters and additional ones are added based on a x^2 minimization scan. The final parametrization is shown in Table 1. Fig. 3 shows the resulted gluon PDF for the 2D measurement (top) and for the 3D measurement (bottom).

Four sources of systematic uncertainties are taken into account for the total PDF uncertainty. The fit uncertainty as estimated by the hessian method, the scale uncertainty by taking a six point variation envelope around the nominal value of μ_R, μ_F, the model uncertainty taken as the sum in quadrature of non-PDF parameter variations (e.g., $\mu_{F,0}$, the strangeness fraction f_s, the charm and bottom quark masses m_c and m_b) and the parametrization uncertainty, again, taking an envelope of all fits performed with one additional E or D parameter than the final parametrization. All sources are added in quadrature to the total PDF uncertainty with the exception of the parametrization one which is added linearly. Fig. 4 shows the individual uncertainty contributions to the gluon PDF for the 2D measurement (top) and for the 3D measurement (bottom).

For the determination of α_S, PDF-only fits are performed using the exact same parametrization as in the PDF+α_S fits. The process is repeated two times, once with the inclusion of the 2D cross sections and once with the 3D cross sections. The resulted values for α_S at the scale of the Z boson mass m_Z are given below:

$$\alpha_S(m_Z) = 0.1201\ (12)_{fit}\ (8)_{scale}\ (8)_{model}\ (5)_{param.}\ (21)_{total}$$

$$\alpha_S(m_Z) = 0.1201\ (10)_{fit}\ (5)_{scale}\ (8)_{model}\ (6)_{param.}\ (20)_{total}$$

The same central value is returned for both cases with the more precise result given by the inclusion of the 3D cross sections. Comparing the values obtained with the inclusion of the dijet cross sections to the current α_S world average ($\alpha_S(m_Z) = 0.1179 \pm 0.0009$) are found to be about one standard deviation away from it.

4. Discussion

The inclusion of CMS dijet cross sections to the HERA DIS data result in further constrained PDF sets. Particularly for the gluon PDF the inclusion of 2D or 3D cross sections leads to a constrained central value in the high-x region ($x > 10^{-1}$). Results are compatible within their respective uncertainties when comparing the fits obtained between the 2D and 3D measurements. Further details can be found in the publicly available Physics Analysis Summary [20].

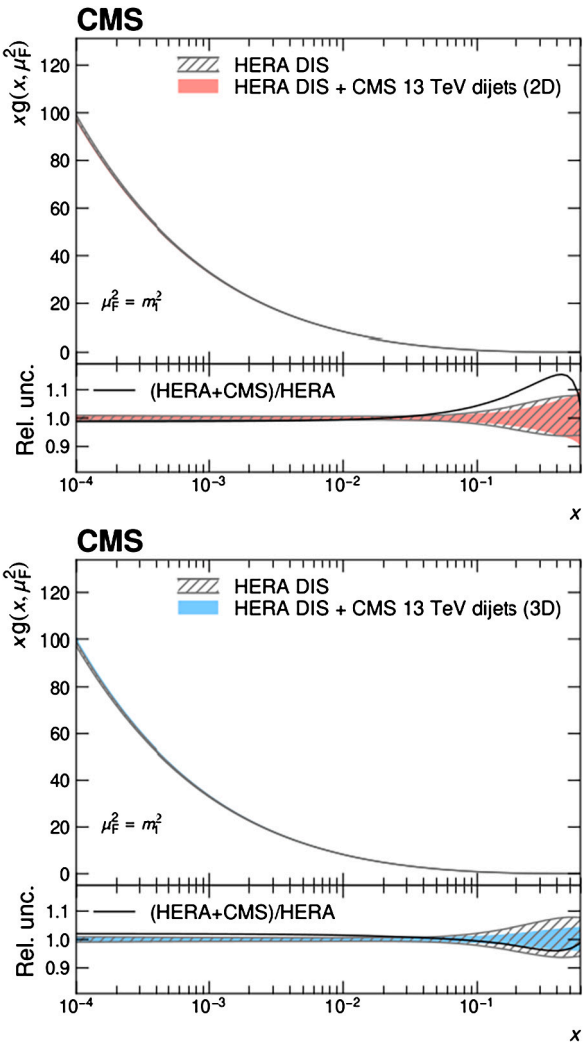

Fig. 3. The gluon PDF with the inclusion of 2D cross sections [20] (top) and with the inclusion of 3D cross sections [20] (bottom).

Further studies are underway for a finer treatment of the QCD analysis. Some examples are further decorrelation of uncertainties for the input tables of the fits, different strategy to estimate the PDF fit uncertainty, ideas of releasing α_S from the start of the overall fit procedure considering it as an additional parameter.

Declaration of competing interest

The authors declare that they have no known competing financial interests or personal relationships that could have appeared to influence the work reported in this paper.

Data availability

The authors do not have permission to share data.

Acknowledgements

We acknowledge support of this work by the project “Dioni: Computing Infrastructure for Big-Data Processing and Analysis.” (MIS No.

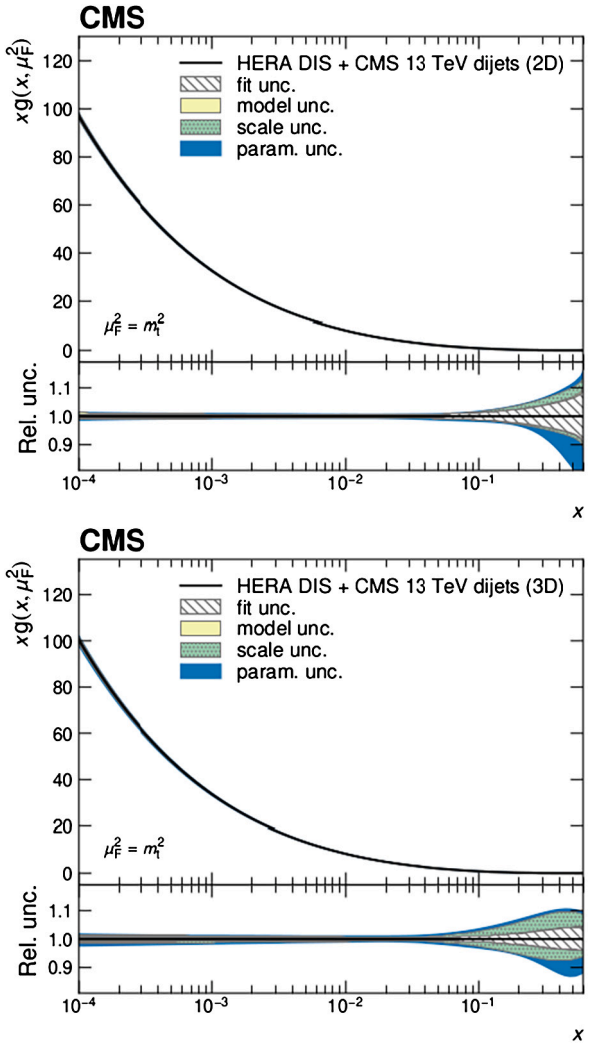

Fig. 4. Individual uncertainty sources on the gluon PDF for the 2D measurement (top) and for the 3D measurement (bottom).

5047222) which is implemented under the Action "Reinforcement of the Research and Innovation Infrastructure", funded by the Operational Programme "Competitiveness, Entrepreneurship and Innovation" (NSRF 2014-2020) and co-financed by Greece and the European Union (European Regional Development Fund).

References

[1] Matteo Cacciari, et al., The anti-kt jet clustering algorithm, J. High Energy Phys. 04 (2008) 063, https://doi.org/10.1088/1126-6708/2008/04/063.

[2] CMS Collaboration, The CMS experiment at the CERN LHC, J. Instrum. 3 (2008) S08004, https://doi.org/10.1088/1748-0221/3/08/S08004.

[3] Torbjörn Sjöstrand, et al., A brief introduction to PYTHIA 8.1, Comput. Phys. Commun. 178 (2008) 852, https://doi.org/10.1016/j.cpc.2008.01.036.

[4] CMS Collaboration, Event generator tunes obtained from underlying event and multiparton scattering measurements, Eur. Phys. J. C 76 (2016), https://doi.org/10.1140/epjc/s10052-016-3988-x.

[5] GEANT4 Collaboration, Geant 4-a simulation toolkit, Nucl. Instrum. Methods, Sect. A 506 (2003) 250, https://doi.org/10.1016/S0168-9002(03)01368-8.

[6] S. Schmitt, TUnfold, an algorithm for correcting migration effects in high energy physics, J. Instrum. 7 (2012) T10003, https://doi.org/10.1088/1748-0221/7/10/T10003.

[7] T. Gehrmann, et al., Jet cross sections and transverse momentum distributions with NNLOJET, PoS RADCOR2017 290 (2018) 074, https://doi.org/10.22323/1.290.0074.

[8] T. Kluge, et al., fastNLO: fast pQCD calculations for PDF fits, in: Proceedings, 14th International Workshop on Deep-Inelastic Scattering (DIS 2006), 2017, p. 483.

[9] D. Britzger, et al., New features in version 2 of the fastNLO project, in: 20th International Workshop on Deep-Inelastic Scattering and Related Subject, 2012, p. 217, http://www.arxiv.org/abs/1208.3641.

[10] D. Britzger, et al., Calculations for deep inelastic scattering using fast interpolation grid techniques at NNLO in QCD and the extraction of α_S from HERA data, Eur. Phys. J. C 79 (2019) 845, https://doi.org/10.1140/epjc/s10052-019-7351-x.

[11] T.-J. Hou, et al., New CTEQ global analysis of quantum chromodynamics with high-precision data from the LHC, Phys. Rev. D 103 (2021) 014013, https://doi.org/10.1103/PhysRevD.103.014013.

[12] S. Dittmaier, et al., Weak radiative corrections to dijet production at hadron colliders, J. High Energy Phys. 11 (2012) 095, https://doi.org/10.1007/JHEP11(2012)095.

[13] J. Currie, et al., Precise predictions for dijet production at the LHC, Phys. Rev. Lett. 119 (2017) 152001, https://doi.org/10.1103/PhysRevLett.119.152001.

[14] A. Gehrmann-De Ridder, et al., Triple differential dijet cross section at the LHC, Phys. Rev. Lett. 123 (2019) 102001, https://doi.org/10.1103/PhysRevLett.123.102001.

[15] S. Alekhin, et al., Parton distribution functions, α_S, and heavy-quark masses for LHC Run II, Phys. Rev. D 96 (2017) 014011, https://doi.org/10.1103/PhysRevD.96.014011.

[16] S. Bailey, et al., Parton distributions from LHC, HERA, Tevatron and fixed target data: MSHT20 PDFs, Eur. Phys. J. C 81 (2021) 341, https://doi.org/10.1140/epjc/s10052-021-09057-0.

[17] NNPDF Collaboration, Parton distributions from high-precision collider data, Eur. Phys. J. C 77 (2017) 663, https://doi.org/10.1140/epjc/s10052-017-5199-5.

[18] H1 ZEUS Collaborations, Combination of measurements of inclusive deep inelastic $e \pm p$ scattering cross sections and QCD analysis of HERA data, Eur. Phys. J. C 75 (2015) 580, https://doi.org/10.1140/epjc/s10052-015-3710-4.

[19] S. Alekhin, et al., HERAFitter: open source QCD fit project, Eur. Phys. J. C 75 (304) (2015), https://doi.org/10.1140/epjc/s10052-015-3480-z.

[20] CMS Collaboration, Multi-differential measurement of the dijet cross section in proton-proton collisions at $\sqrt{s} = 13$ TeV, CMS-PAS-SMP-21-008, https://cds.cern.ch/record/2843201, 2022.